Electronic Supplementary Material (ESI) for Energy & Environmental Science.
This journal is © The Royal Society of Chemistry 2023

Electronic Supplementary Material (ESI) for Energy & Environmental Science.

Supplementary Information

Facet-Controlled Bifunctional WO_3 Photocathodes for High-Performance Photo-assisted Li-O_2 Battery

Meng Wang,[‡a,b] Jie Chen,[‡a,c] Zhangliu Tian,[‡*b] Wenrui Dai,[b,f] Baihua Cui,[a,b] Xinhang Cui,[b] Dong Wang,[g] Yukun Xiao,[a,b] Xu Lian,[b] Chonglai Jiang,[a,b] Haotian Yang,[a,b] Yihe Wang,[a,b] Zejun Sun,[b] Yishui Ding,[a,b] Yi-Yang Sun,[d] Jia Zhang,[e] Wei Chen*[a,b,c]

[a] Joint School of National University of Singapore and Tianjin University, International Campus of Tianjin University, Binhai New City, Fuzhou, 350207, China
[b] Department of Chemistry, National University of Singapore, 3 Science Drive 3, 117543, Singapore
[c] Department of Physics, National University of Singapore, 2 Science Drive 3, 117542, Singapore
[d] State Key Laboratory of High Performance Ceramics and Superfine Microstructure, Shanghai Institute of Ceramics, Chinese Academy of Sciences, Shanghai 201899, P. R China
[e] Institute of High Performance Computing, A*STAR (Agency for Science, Technology and Research),138632, Singapore
[f] School of Materials and Chemistry, University of Shanghai for Science and Technology, Shanghai 200093, P. R China
[g] Center for High Pressure Science and Technology Advanced Research, Beijing 100094, P. R China
‡ These authors contributed equally to this work.

*Correspondence: tianzl@nus.edu.sg; phycw@nus.edu.sg.

Supplementary Experimental Section

Chemicals and materials

Ammonium Paratungstate (99 %),Tungstic Acid (99 %), Poly (Vinyl Alcohol) (PVA, 99 %+), Dimethyl Carbonate (anhydrous, ≥99 %), Dimethyl Sulfoxide (DMSO, 99.9 %), Tetrabutylammonium Perchlorate ($TBAClO_4$, 99 %), Acetonitrileand (MeCN, anhydrous, 99.8 %), Silver Nitrate ($AgNO_3$, ≥99 %), Triethylene Glycol Dimethyl Ether (TEGDME, anhydrous, ≥99 %), Lithium Trifluoromethanesulfonate (CF_3SO_3Li, 99.9 %), Ammonium trifluoromethanesulfonate ($CF_3SO_3NH_4$, 99%) and Nafion (Dupont, 5 wt %) were purchased from SIGMA-ALDRICH Pte Ltd. Acetonitrile (HPLC, 99.9 %) was obtained from Anhui Fulltime Specialized Solvents & Reagents Co., Ltd. Hydrochloric acid (37 % wt) and Hydrogen Peroxide (30 wt %) were obtained from VWR Singapore Pte Ltd. Carbon Cloth (CC) (WOS1009) was purchased from CeTech Co., LTD. All the chemicals used throughout this work were used as received without any further purification.

DFT computational details

The DFT calculations were performed with the VASP code (version 6.3.0). The monoclinic WO_3 structure containing 8 formula units was obtained from the ICSD database and further optimized using the R2SCAN functional matching the accuracy of the parent SCAN functional,[1-3] which is often utilized to study the transition metal oxide systems.[4-6] The comparisons of optimized and experimental lattice constants are in **Table S1**. After obtaining the optimized WO_3 bulk structure, we constructed the (002) and (020) slab models, which contain two unit cells along the direction normal to the surface. The lengths of vacuum in the slabs are more than 14 Å. We considered different coverages of the terminal O atoms on the surface by calculating the corresponding formation energies as a function of O chemical potential according to[7, 8]

$$E_{\text{form}} = E_{x\text{O}} - E_{0\text{O}} - x\,(E_{\text{O}} + \mu_{\text{O}}),$$

where $E_{x\text{O}}$ and $E_{0\text{O}}$ are the total energies of slab models with x and zero terminal O atoms, respectively. E_{O} is the total energy per O atom in an O_2 molecule. μ_{O} is the chemical potential of O. As the reaction was carried out with the presence of strong oxidant H_2O_2, we considered the O-rich condition, i.e., μ_{O} = 0 eV. Our results show that the most stable structures for both the (002) and (020) slabs have 50% terminal O atoms on the surface, as shown in **Fig. S1**.

After determining the coverage of terminal O on the surface, the WO_3 (020) and (002) surface models were optimized by fixing the bottom W-O octahedral layer. The adsorption of the LiO_2 cluster on the WO_3 surface was realized by attaching the Li atom to a terminal O atom and the pair of O_2 to a W atom, as shown in **Fig. 2** in the main text. Different adsorption configurations were tested and the most energetically favourable configurations were utilized to calculate the adsorption energies.

The adsorption energies are calculated by

$$\Delta G_{\text{ads}} = G(\text{LiO}_2@\text{WO}_3) - G(\text{LiO}_2) - G(\text{WO}_3)$$

where $G(\text{LiO}_2@\text{WO}_3)$, $G(\text{LiO}_2)$ and $G(\text{WO}_3)$ are the free energies of the adsorption structures, the LiO_2 cluster and the bare WO_3 slab. The free energies are calculated as the following equation,

$$G = E + ZPE + \Delta U - T{\cdot}S$$

where E is the total energy, ZPE the zero-point energy, ΔU the thermodynamic correction contributed from thermal capacity and $T{\cdot}S$ the entropy with T at the room temperature. In the calculation of thermodynamic correction, the atoms of the substrates are fixed. When calculating the total energy, we considered the correction of solvent effect by using the implicit solvent model, which is implemented in the VASPsol code.[9, 10] A dielectric constant of 7.79 was used to describe the TEGDME electrolyte. The solvation energy of the LiO_2 cluster is calculated by the free energy difference between the LiO_2 cluster in the TEGDME electrolyte and in vacuum.

The plane-wave cut off energy was 612 eV in optimizing the bulk structure and 408 eV in optimizing the slab models. The Monkhorst−Pack grid for k-points was 3 × 3 × 3 in the optimization of bulk structure and 3 × 3 × 1 in the optimization of the slab models. Γ-point was used for the LiO_2 cluster. The energy criterion for the convergence of self-consistent calculation was 1.36×10^{-5} eV and the

criterion for the force convergence was 0.0257 eV/Å.

Assembly and test of Li-O_2 cells

Li-O_2 cells were assembled based on 17 holes CR2032 type coin cells for all electrochemical tests. Lithium metal was applied as the anode, and one piece of glass fiber membrane soaked with 1 M $LiCF_3SO_3$/TEGDME as electrolyte was used as the separator. The cathode was fabricated by growing WO_3 on a CC current collector. And the semiconductor/CC layer of the cathode was exposed to outward to receive illumination. After being assembled in an Ar-filled glovebox, the cell was transferred to a sealed photoreactor and purged the reactor for 20 min with oxygen flow under ambient pressure. The discharge/charge tests were conducted at room temperature on the LAND multi-channel battery testing unit. To avoid the thermal effect of the Xenon lamp, a specially designed battery test cell with good heat dissipation was used. The volatilization of the electrolyte can be effectively reduced by changing the size of the quartz window and the volume of the battery test cell. Linear sweep voltammetry (LSV), cyclic voltammetry (CV) of the cell were conducted on a Multi Autolab electrochemical workstation at a scan rate of 0.1 mV/s.

Electrochemical characterizations

A CHI760E electrochemistry working station was used for the electrochemical test of the Mott-Schottky and open circuit potential (OCP). The measurement of the Mott-Schottky was investigated by employing a three-electrode system in 0.5 M Na_2SO_4 solution. WO_3/CC was used as the working electrode, with a Pt sheet counter-electrode and Ag/AgCl reference electrode. The plots were converted from impedance-potential curves conducted at a frequency of 1 kHz without illumination. Furthermore, the OCP of the WO_3/CC photocathode was performed in TEGDME with and without illumination. In a typical three-electrode system, WO_3/CC was used as the working electrode, with a Pt sheet counter-electrode and a non-aqueous Ag/Ag^+ (0.01 M $AgNO_3$ in 0.1 M $TBAClO_4$-MeCN) reference electrode. The potential of the reference electrode was calibrated by the ferrocene/ferricenium (Fc/Fc^+) redox couple in TEGDME, and a 300 W xenon lamp fitted with an AM 1.5 filter was used to simulate sunlight.

Gas chromatography (GC) tests for the recharging Li-O_2 batteries under illumination

To analyze the decomposition of Li_2O_2, the battery was first discharged under O_2. Then, the battery test cell was refilled by Ar for the charging process. After the battery was recharged, the generated gas was injected into GC under the blow of Ar for further detection. The decomposed products were analyzed by the thermal conductivity detector (TCD).

UV-vis spectroscopy measurement of O_2^- generation under illumination

KO_2 was dissolved in TEGDME-methanol as O_2^- standard to determine the absorption peak position, where methanol acts as a hole scavenger. For the electrolyte control group, the TEGDME-methanol was purged with Ar for 30 min. Then, it was exposed to light under Ar flow for 10 min and transferred to a cuvette for UV testing. For the sample measurement under dark conditions, the WO_3/CC cathode was immersed in TEGDME-methanol and purged with O_2 for 30 min. Then, the solution was quickly transferred to a cuvette for UV testing. Similarly, the O_2^--saturated sample cell was exposed to light for 10 min for further analysis.

Evaluation of O_2^- adsorption capacity on WO_3 surface

The O_2^- surface adsorption ability was evaluated by rotating ring-disk electrodes (RRDE) and UV-vis spectroscopy.
The RRDE test with a 4 mm in diameter glassy carbon disk surrounded by a Pt ring (ring electrode:

d_{inside} = 4.3 mm, $d_{outside}$ = 6.3 mm) was performed on a RRDE type rotating ring disk electrode (TAIZHOU KERUITE ANALYTICAL INSTRUMENT Co., LTD) coupled with a CHI760E workstation. The ring electrode collection efficiency ($N_{theoretical}$ =25%) is determined by using a ferrocene/ ferricenium (Fc/Fc^+) redox couple. In the O_2 saturated $LiCF_3SO_3$/TEGDME electrolyte, LiO_2 forms at the disk, the soluble LiO_2 species could be transferred to the Pt ring and formed ring current during the discharging process. Therefore, the intensity of the ring current was invisible with the O_2^- surface adsorption ability.[11] The WO_3 inks were prepared by mixing 5 mg WO_3, 50 μL Nafion (Dupont, 5 wt%), and 950 μL water with 1 h ultrasonic treatment. A 3.5 μL WO_3 ink was dropped onto the GC electrode and dried at room temperature. For the RRDE measurement, a Pt sheet was served as a counter electrode and a non-aqueous Ag/Ag^+ (0.01 M $AgNO_3$ in 0.1 M $TBAClO_4$-MeCN) was employed as the reference electrode. The potential of the reference electrode was calibrated before the measurement. The RRDE curves were recorded by a CHI760E bipotentiostat at 1600 rpm with a scan rate of 10 mV s^{-1} and the Pt ring electrode was biased to 3.5 V vs. Li^+/Li. The electrolyte (1 M $LiCF_3SO_3$-TEGDME) was saturated with O_2 for 30 min before use, and the test was performed under continuous O_2 flow.

For the UV-vis measurement, the O_2^- adsorption efficiency was evaluated by comparing the UV intensity before and after KO_2 adsorption.[12] Specifically, the 5-fold diluted saturated KO_2/DMSO solution was performed as a blank control sample, and the absorbance intensity of O_2^- was recorded as I_0 after stirring for 3 h. In addition, 10 mg WO_3 was mixed with 3 mL of diluted KO_2/DMSO for 3 h stirring, followed by centrifugation to obtain the supernatant. The absorbance intensity of O_2^- after the adsorption experiment was denoted as I_1. The O_2^- adsorption efficiency was calculated according to the following equation: $E\ (\%) = (I_0 - I_1)/I_0 * 100\ \%$.

The optical properties of commercial Li_2O_2

The RDE test with a 4 mm in diameter glassy carbon disk was performed on a RRDE type rotating ring disk electrode (TAIZHOU KERUITE ANALYTICAL INSTRUMENT Co., LTD) coupled with a CHI760E workstation. After drop the WO_3 ink on the GC electrode (the detailed experimental process was the same as the above RRDE test), the RDE curves were recorded by a CHI760E at 1600 rpm with a scan rate of 10 mV s^{-1} with and without illumination.

In the potentiostatic deposition experiment, the 5 mm in diameter Au disk electrode was used as the working electrode and the Li foil was used as the reference and the counter electrodes. A 4 μL WO_3 ink was dropped onto the Au electrode and dried at room temperature. Then, the Au and Au/WO_3 disk electrodes were held at 2.5 V vs. Li^+/Li for 1 h to deposit Li_2O_2. Notably, the electrodes were spinning at a high rate of 3000 rpm to ensure a dense Li_2O_2 film cotaed on the disk. After the deposition of Li_2O_2, the I-t curves of the electrodes with interval irradiation were also held at 2.5 V to collect the results.

The measurement of the Mott-Schottky was investigated by employing a three-electrode system in the acetonitrile solution of ammonium trifluoromethanesulfonate.[13] Commercial Li_2O_2 powder was pressed into a thin sheet as the working electrode, with a Pt sheet counter-electrode and a non-aqueous Ag/Ag^+ (0.01 M $AgNO_3$ in 0.1 M $TBAClO_4$-MeCN) reference electrode. The plots were converted from impedance-potential curves conducted at a frequency of 1 kHz without illumination and the three-electrode system were prepared in a glove box filled with Ar.

Table S1. The comparison of monoclinic WO_3 lattice constants from calculation and experiment.

	a / Å	**b / Å**	**c / Å**	**β /**
Experiment	7.297	7.539	7.688	90.91
Calculation	7.476	7.441	7.599	91.10

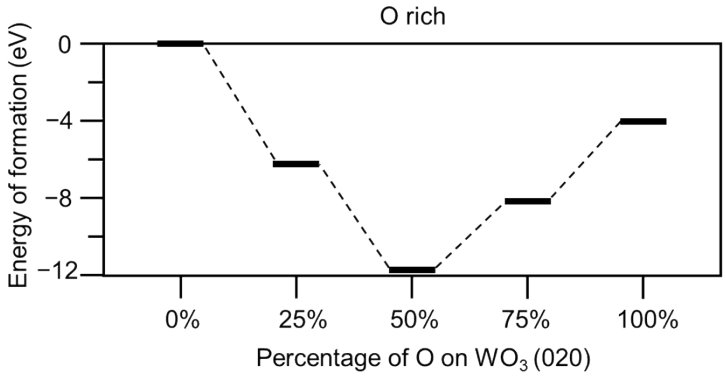

WO_3	Energy of formation / eV	
Coverage	(020)	(002)
0%	0	0
25%	-6.56	-6.72
50%	-11.80	-12.31
75%	-8.37	-8.36
100%	-4.22	-4.46

Figure S1. Formation energies of WO_3 (020) surfaces and (002) surfaces with different coverages of terminal O atoms under the O-rich condition. Figure shows the formation energies of (020) surfaces. Data of formation energies of the (020) and (002) surfaces are listed in the right table. The surfaces with zero terminal O atoms were taken as the reference.

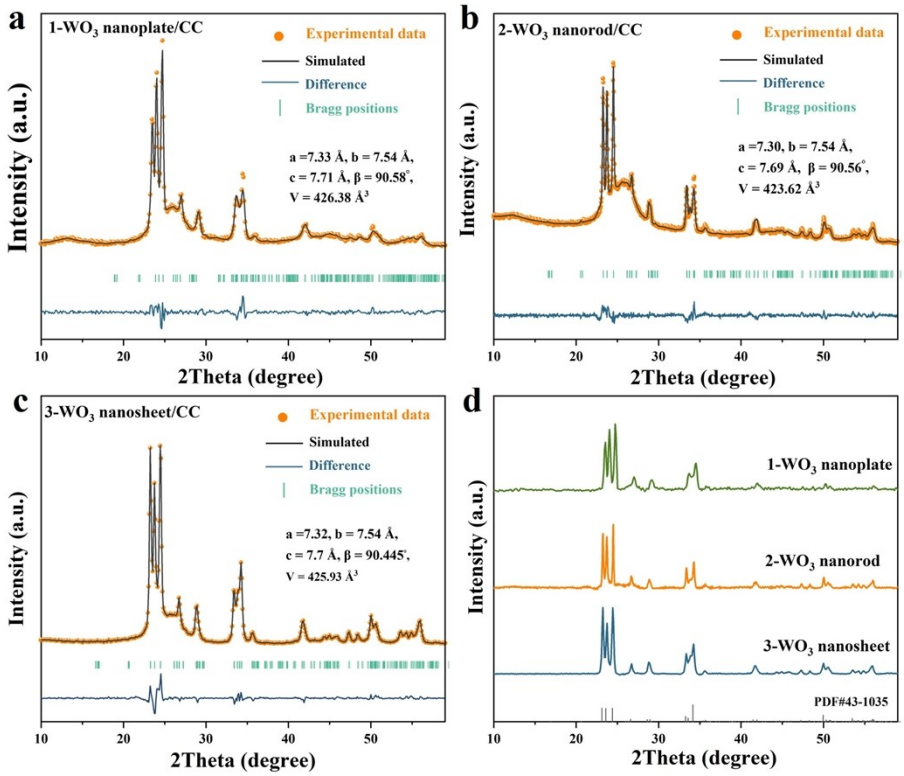

Figure S2. XRD patterns of (a) 1-WO_3 nanoplate/CC, (b) 2-WO_3 nanorod/CC and (c) 3-WO_3 nanosheet/CC using Rietveld refinement method. (d) The baseline corrected XRD spectra of prepared WO_3 photocathodes.

According to the refinement data, all the samples crystallize in the monoclinic phase with the *P*21/*n* space group. The lattice parameters and refinement data are shown in **Table S2**.

Table S2. The lattice parameters and refinement data of different WO_3.

Sample	Space group	*a* (Å)	*b* (Å)	*c* (Å)	*β* (°)	*V* (Å^3)	R_{wp} (%)	R_p (%)	χ^2 (%)
1-WO_3	*P*21/*n*	7.33	7.54	7.71	90.58	426.38	6	4.65	2.24
2-WO_3	*P*21/*n*	7.3	7.54	7.69	90.56	423.62	3.3	2.47	2.26
3-WO_3	*P*21/*n*	7.32	7.54	7.7	90.445	425.93	6.58	5.24	5.02

The results proved that the three WO_3 photocathodes have similar lattice parameters.
The morphology of the crystal is related to the crystal plane preferred orientation, and the difference in the preferred orientation of the crystal plane will directly affect the properties. In general, Rietveld refinement requires the sample to be well-ground to eliminate the preferred orientation as much as possible in order to obtain a correct structure model. For unground powder samples, a preferred orientation coefficient is sometimes added to correct the structure model, which no longer has the real morphology information. Therefore, to reliably demonstrate the exposed crystal planes ratio of the three samples, we removed the diffraction background of the carbon cloth, and then calculated the crystal plane information. The facet intensity ratios of the three photocathodes are obtained directly from the baseline corrected XRD spectra (**Fig. S2d**). Accordingly, the 3-WO_3 nanosheet possesses the highest intensity ratio of (002)/(020) facet (1.24), while the 2-WO_3 nanorod and 1-WO_3 nanoplate exhibit the intensity ratio of (002)/(020) facet of 1.05 and 0.85, respectively.

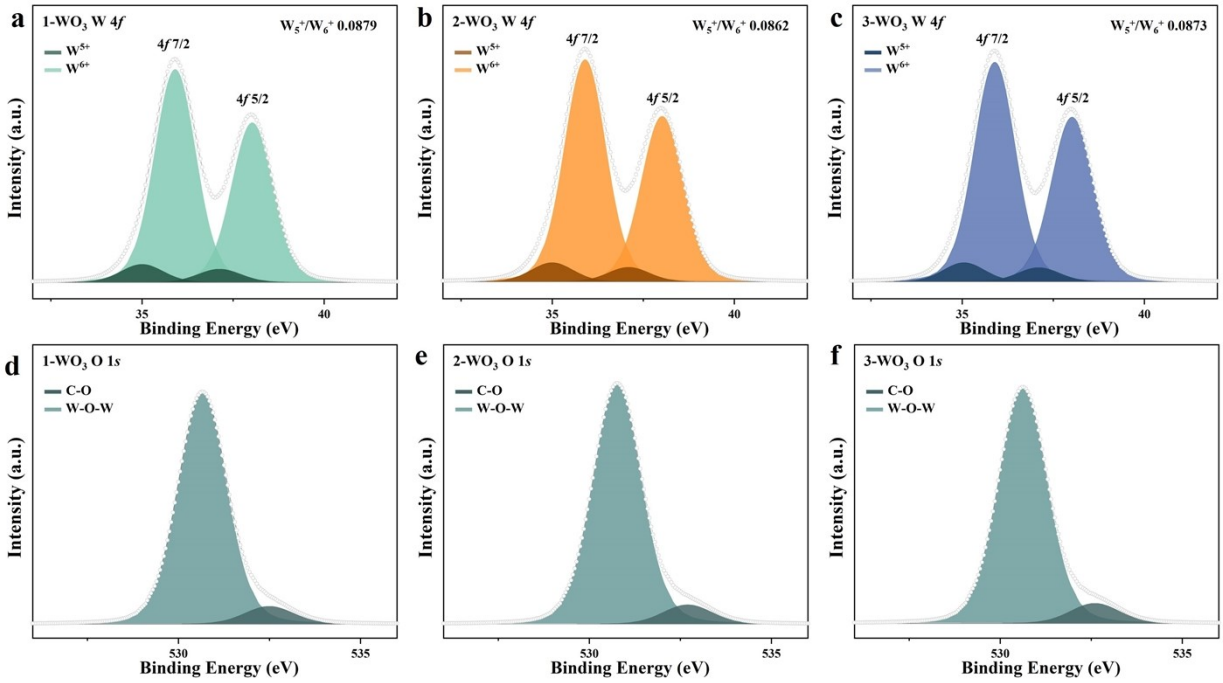

Figure S3. WO_3 XPS spectra of W 4*f* and O 1*s*.

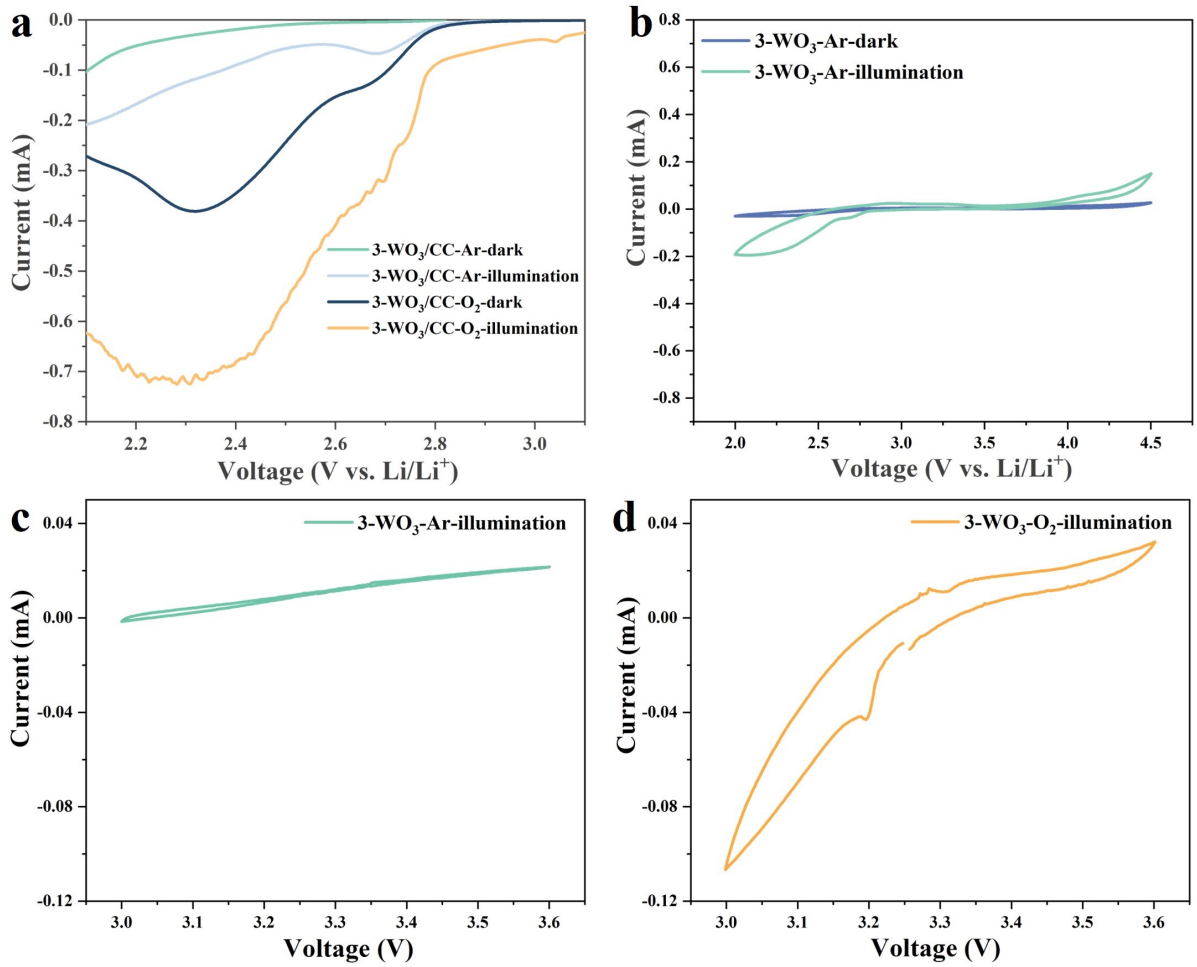

Figure S4. (a) Cathodic LSV curves of the Li–O_2 batteries with and without illumination at a scan rate of 0.1 mV s^{-1}. (b) Cathodic CV curves of 3-WO_3/CC under Ar atmosphere with and without illumination at a scan rate of 0.1 mV s^{-1}. Cathodic CV curves of 3-WO_3/CC under (c) Ar and (d) O_2 atmosphere within 3.0 V-3.6 V at a scan rate of 0.1 mV s^{-1}.

The absence of significant cathodic current under Ar (**Fig. S4a-b**) suggests that the photoelectrons are mainly accelerating the ORR reaction. Besides, in order to match the actual charge and discharge process, the CV test is also performed within 3.0-3.6 V (**Fig. S4c-d**) (The range of charging and discharge voltage is between 3-3.6 V for the three photocathodes (**Fig. 4a**)). The result indicates that the side reactions are ignorable in the charge and discharge process.

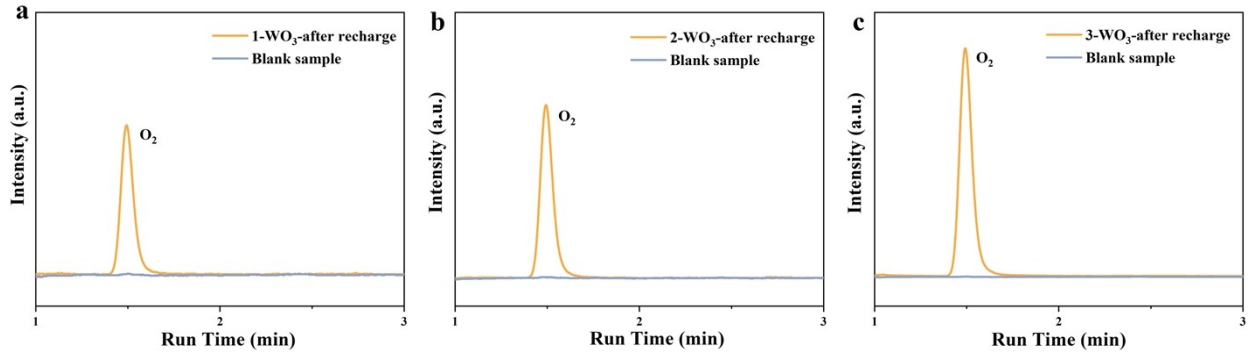

Figure S5. (a-c) GC plots of the recharged Li-O_2 battery with different photocathodes under illumination.

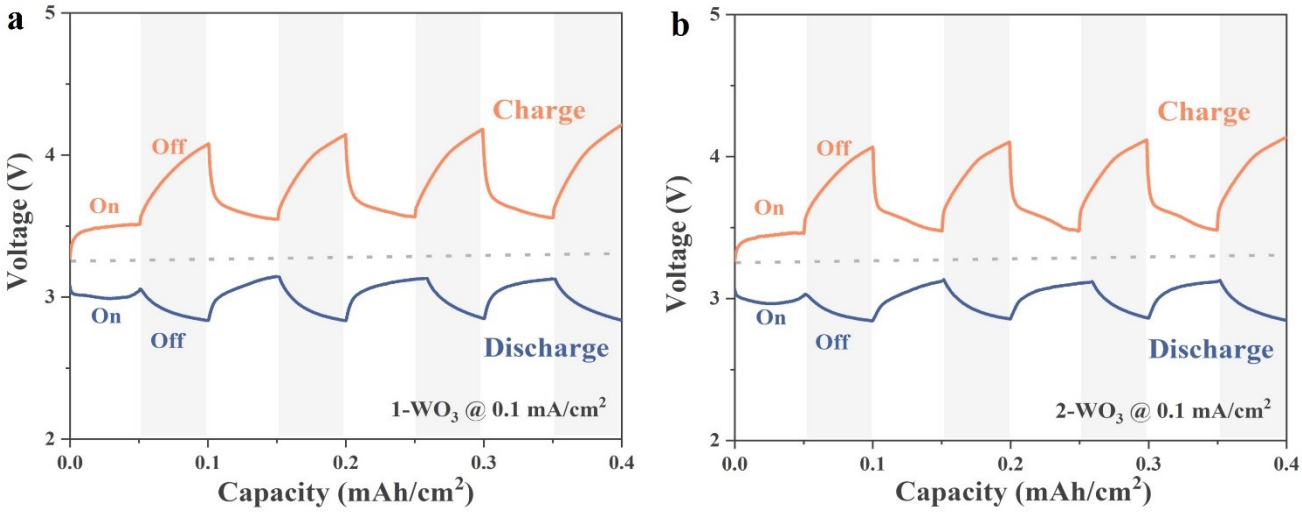

Figure S6. Photo responses of the Li-O_2 batteries with intermittent light on and off in both the discharge and charge processes for (a) 1-WO_3-nanoplate/CC and (b) 2-WO_3-nanorod/CC.

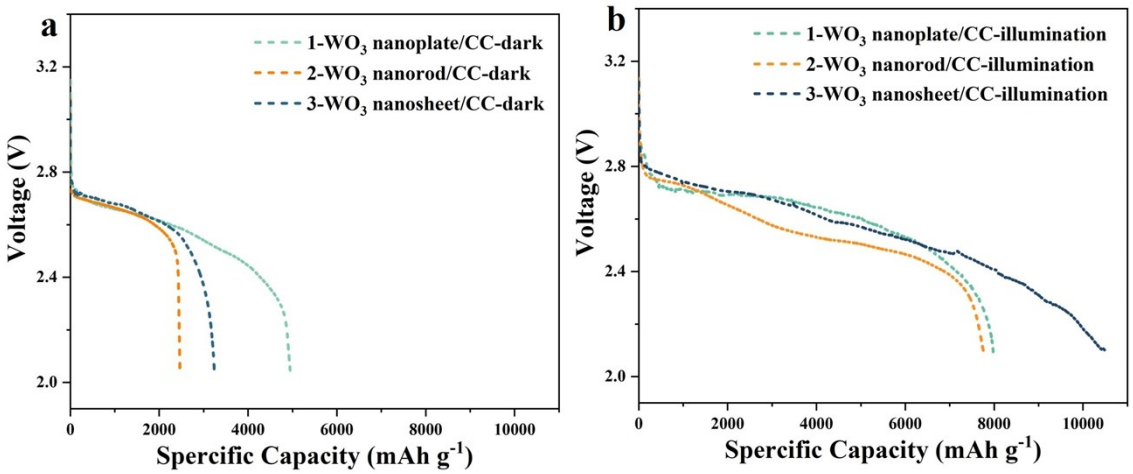

Figure S7. Galvanostatic discharge profiles of the three photocathodes at 50 mA g^{-1} (0.02 mA/cm^2) (a) without and (b) with illumination.

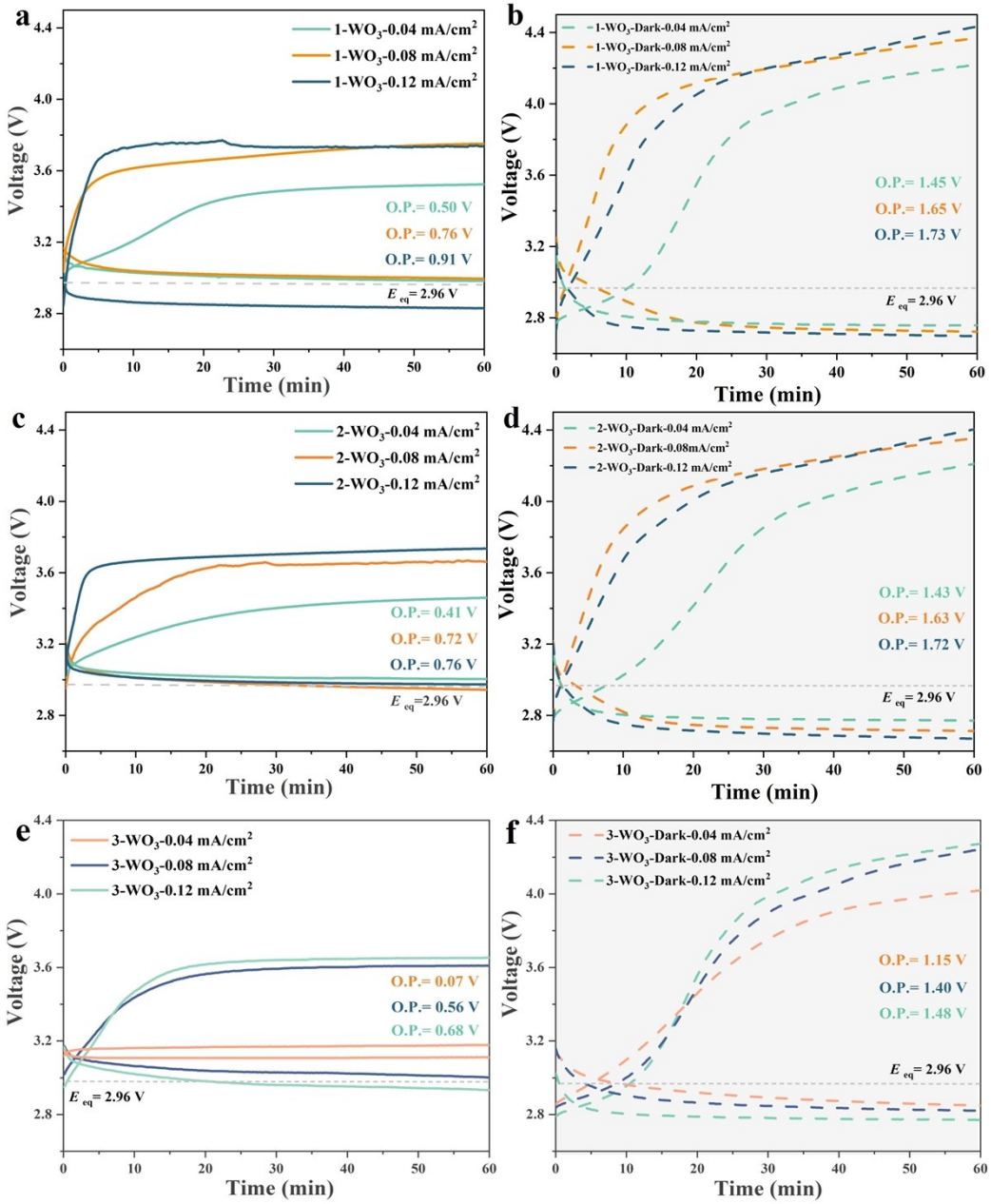

Figure S8. The discharge and charge profiles of 1-WO_3-nanoplate/CC, 2-WO_3-nanorod/CC and 3-WO_3-nanosheet/CC at different current densities with (a), (c), (e) and without (b), (d), (f) illumination.

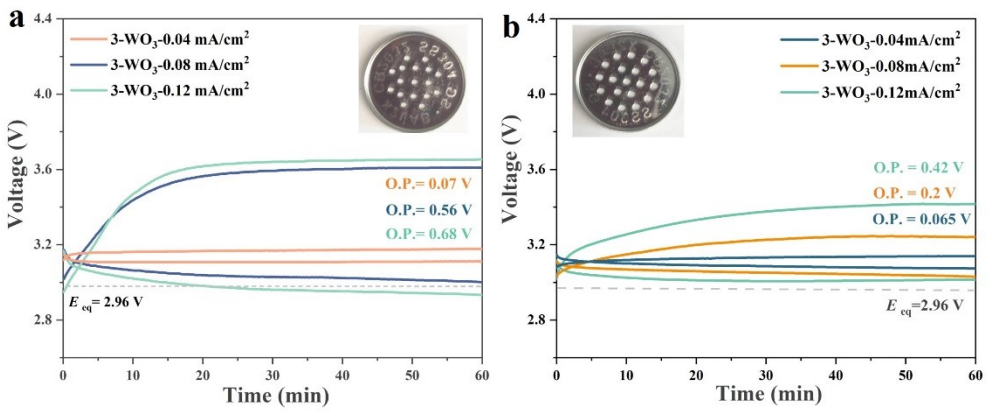

Figure S9. Rate performance for 3-WO_3 nanosheet photocathode with (a) 17 holes (hole diameter = 1 mm) CR2032 type coin cell and (b) 19 holes (hole diameter = 1.5 mm) CR2032 type coin cell.

The discharge-charge process of photo-assisted Li-O_2 battery is determined by the photoreaction and electrochemical routes. When the current density is small, the photoreaction route will dominate the reaction, and thus the discharge/charge voltages close to the theoretical values under illumination. As the current density increases, the proportion of the electrochemical route will increase to sustain the discharge-charge process, leading to a large overpotential. Therefore, the rate performance is determined by the amount of photoexcited carriers. To minimize the volatilization of the electrolyte, the 17 holes (hole diameter = 1 mm) CR2032 type coin cell was used for the battery assemble (Inset of **Fig. S9a**). After replacing the cathode shell by the 19 holes (hole diameter = 1.5 mm) CR2032 type coin cell, the polarization overvoltage can be reduced from 0.68 V (0.12 mA cm^{-2}), 0.56 V (0.08 mA cm^{-2}) and 0.07 V (0.04 mA cm^{-2}) to 0.42 V (0.12 mA cm^{-2}), 0.2 V (0.08 mA cm^{-2}) and 0.065 V (0.04 mA cm^{-2}), respectively (**Fig. S9b**). The prominently enhanced rate performance is ascribed to the increased light-received area, resulting in the increased photocurrents for both ORR and OER. A small light-received area will lead to a weaker photo effect on tuning the polarization under increased current densities. Considering that this work is mainly focused on the structure-activity relationship between photocatalytic materials and charge-discharge mechanisms in photo-assisted Li-O_2 battery, all battery performance tests were performed by the 17 holes (hole diameter = 1 mm) CR2032 type coin cell to reduce the effect of volatilization of electrolytes as much as possible.

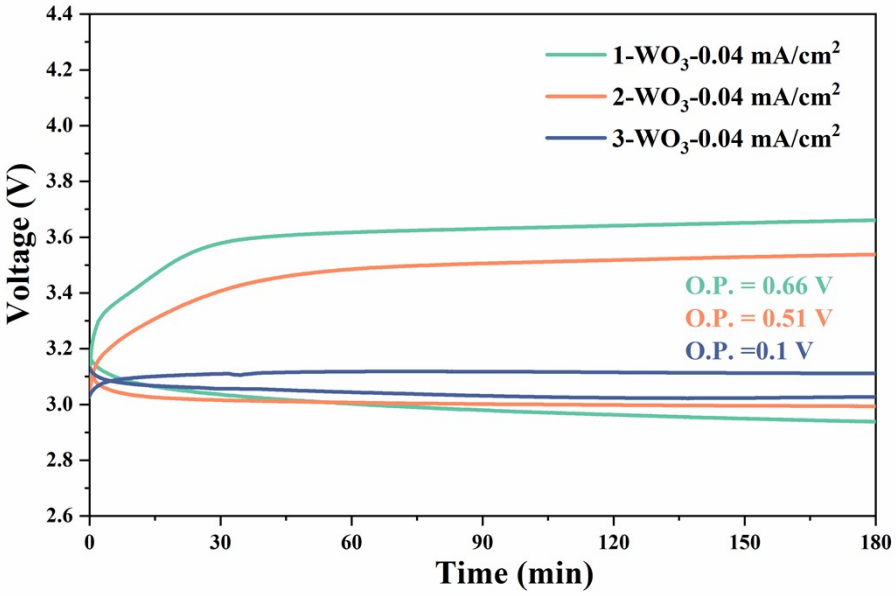

Figure S10. 3h discharge and charge curves of WO_3/CC at 0.04 mA cm^{-2}.

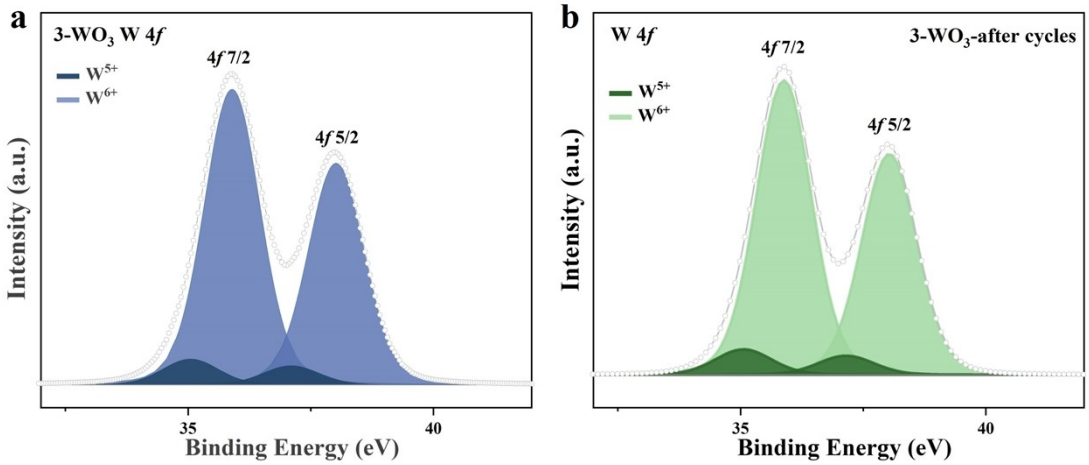

Figure S11. The comparison of XPS spectra of the 3-WO_3 (a) before and (b) after the 50th CV test under illumination.

Table S3. The ICP result of electrolyte after 50th CV cycle collected from the 3-WO_3 photoelectrode under illumination.

Element	Determined Values (ppm)
W	No

Table S4. Performance comparison of facet-controlled WO_3 with reported semiconductor photocathodes for Li-O_2 batteries.

Photocatalyst	Current Density (mA cm^{-2})	Charge Voltage (V)	Discharge Voltage (V)	Capacity	Cycles	Ref.
WO_3 nanosheet	**0.04**	**3.17**	**3.1**	**10500 mAh g^{-1} @0.02 mA/cm^2 (film-growth)**	**100@0.04 mA/cm^2**	**This work**
NiO (Magnetic and Optical)	0.01	2.73	2.64	---	60 (MF=5 mT)	*Adv. Mater.*, 2022, **34**, 2104792.
$MoS_2/ZnIn_2S_4$	0.05	3.29	3.18	2.05 mAh cm^{-2}	65	*Carbon Energy*, 2022, **4**, 1169–1181.
Black TiO_2 (solid-state battery)	0.01	3.16	2.85	2688 mAh $g_{TiO2}{}^{-1}$ @ 0.05 mA cm^{-2}	90 @0.05 mA/cm^2	*Nano Energy*, 2022, **98**, 107248.
Fe_2O_3/C_3N_4	0.1	3.13	3.19	---	50 @0.4 mA/cm^2	*Angew. Chem. Int. Ed.*, 2022, **61**, e202116699.
Ov-TiO_2-650	100 mA/g	3.56	2.86	9390 mAh/g @ 100 mA/g	100 @ 500 mA/g with capacity limit of 1000 mAh/g	*Chinese Chem. Lett.*, 2022, **33**, 4008–4012.
$CsPbBr_3$@PCN-333	0.01	3.44	3.19	---	100	*J. Am. Chem. Soc.* 2021, **143**, 14253.
Co-TABQ/CP	0.1	3.32	3.12	---	50 @0.3 mA/cm^2	*J. Am. Chem. Soc.,* 2021, **143**, 1941-1947
TiO_2/Fe_2O_3	0.01	~3.25	~3.06	---	100	*Adv. Mater*., 2020, **32**, 1907098.
C_3N_4	0.04	3.38	3.22	---	10 @0.1 mA/cm^2	*Angew. Chem. Int. Ed.*, 2019, **58**, 19021–19026.
WO_3 nanowire arrays	0.06	3.55	2.75	---	100	*ACS Sustain. Chem.* Eng., 2019, **7**, 5931.

Note: All of the above battery performance were obtained directly from the articles or converted based on the given data.

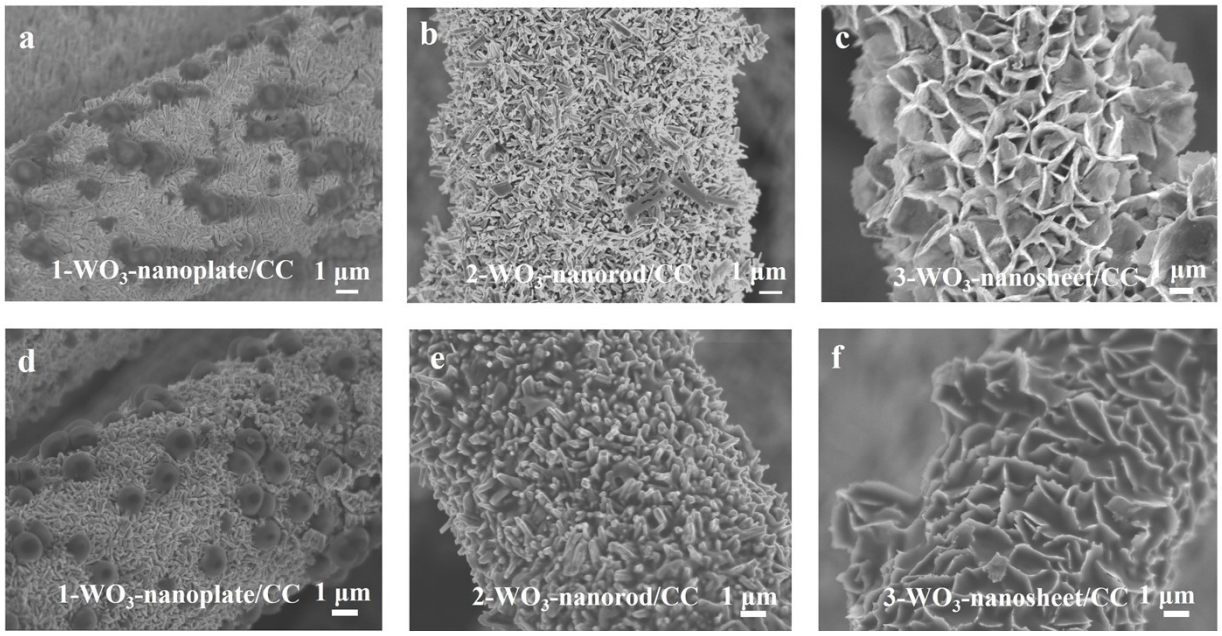

Figure S12. SEM image of 1-WO_3, 2-WO_3 and 3-WO_3 after discharge process at a current density of (a-c) 0.04 mA cm^{-2} and (d-f) 0.08 mA cm^{-2}.

Table S5. The specific surface areas for the fabricated WO_3 photocathodes.

Photocathode	Specific surface area m^2/g
1-WO_3 nanoplate/CC	72.5
2-WO_3 nanorod/CC	67.5
3-WO_3 nanosheet/CC	73.6

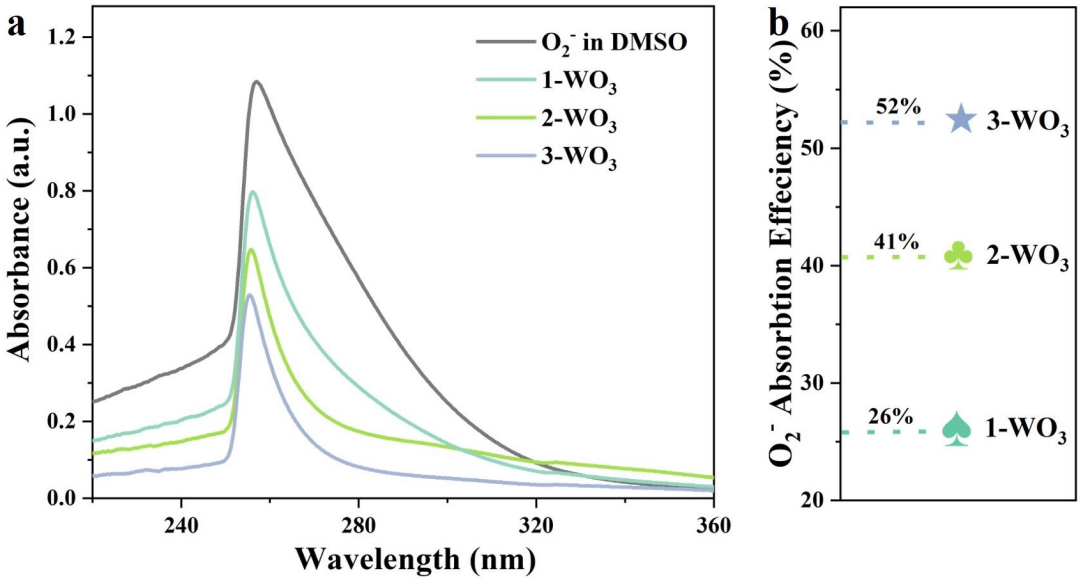

Figure S13. (a) UV-vis spectra of the KO_2/DMSO solution before and after the adsorption experiments with the addition of 1-WO_3, 2-WO_3 and 3-WO_3, respectively. (b) the corresponding O_2^- adsorption efficiencies for 1-WO_3, 2-WO_3 and 3-WO_3 calculated from the UV-vis spectra.

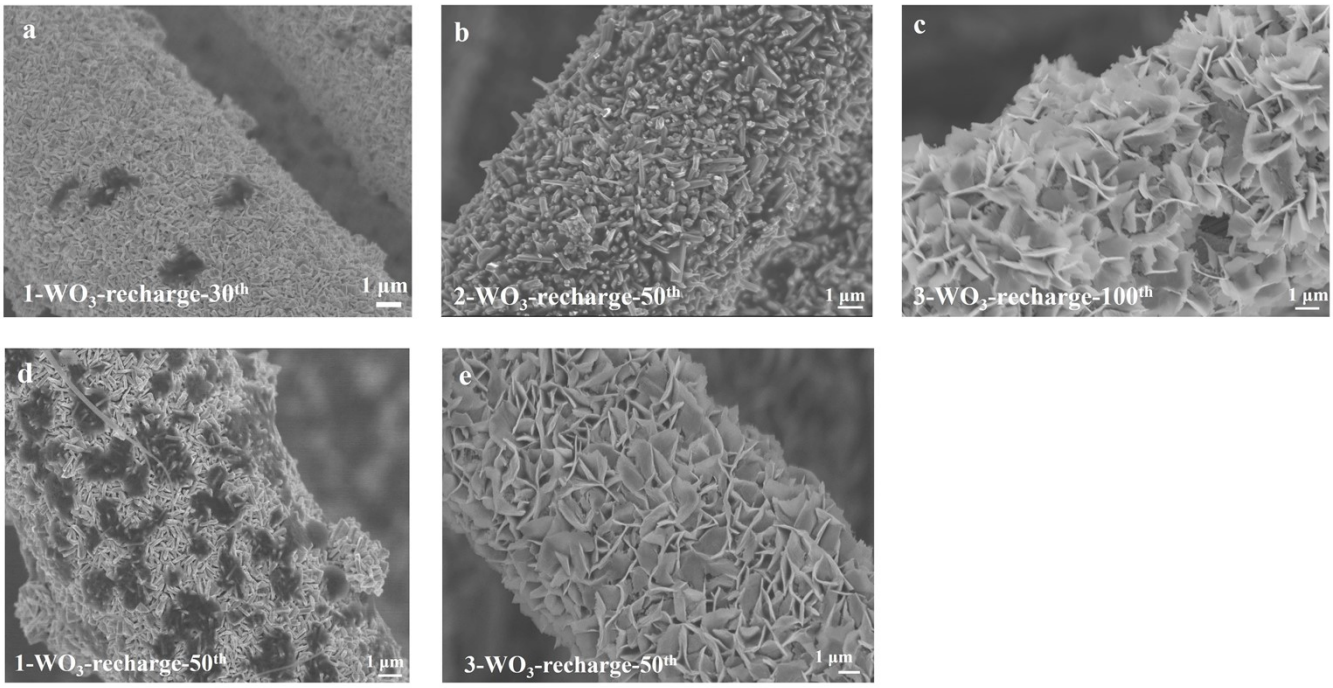

Figure S14. (a) SEM images of 1-WO_3-nanoplate/CC after the 30th charging process at a current density of 0.04 mA cm^{-2}. (b) SEM images of 2-WO_3-nanorod/CC after the 50th charging process at a current density of 0.04 mA cm^{-2}. (c) SEM images of 3-WO_3-nanosheet/CC after the 100th charging process at a current density of 0.04 mA cm^{-2}. (d-e) SEM images of 1-WO_3-nanoplate/CC and 3-WO_3-nanosheet/CC after the 50th charging process at a current density of 0.04 mA cm^{-2}.

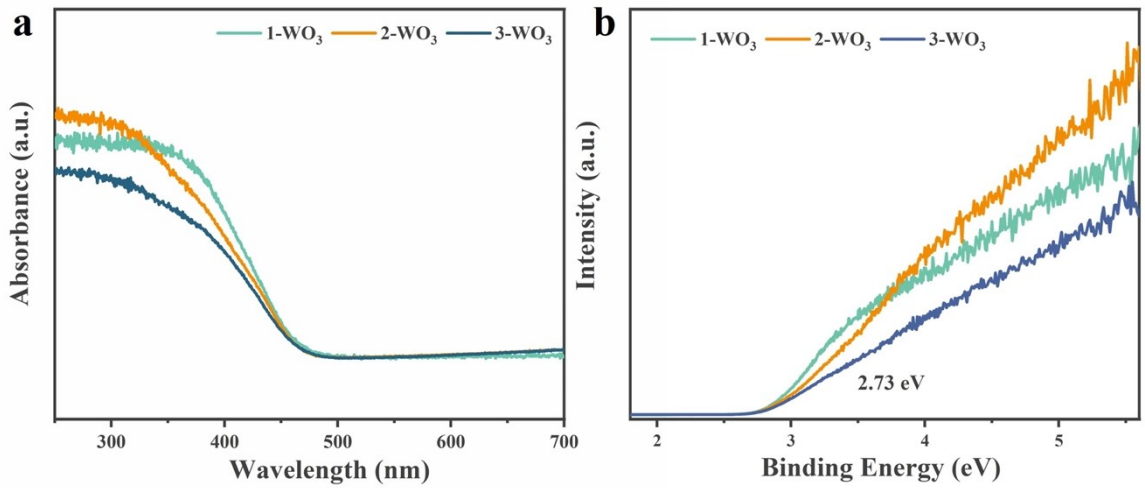

Figure S15. (a) UV−visible absorption spectra. (b) Tauc plots of prepared WO_3/CC photocathodes.

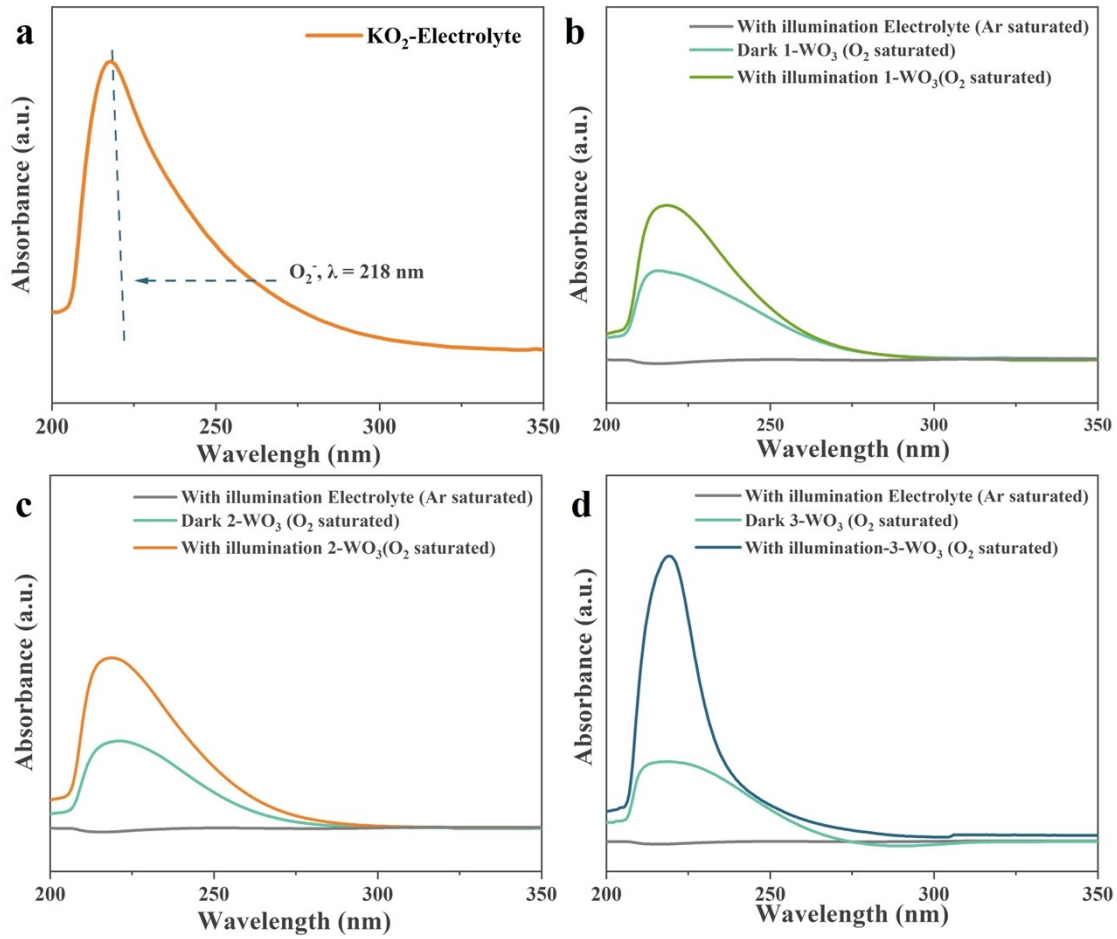

Figure S16. (a) UV–vis spectrum of KO_2-TEGDME-Methanol. (b-d) UV–vis spectra of the Ar saturated TEGDME-Methanol under illumination and O_2 saturated electrolyte with different WO_3 cathodes before and after illumination.

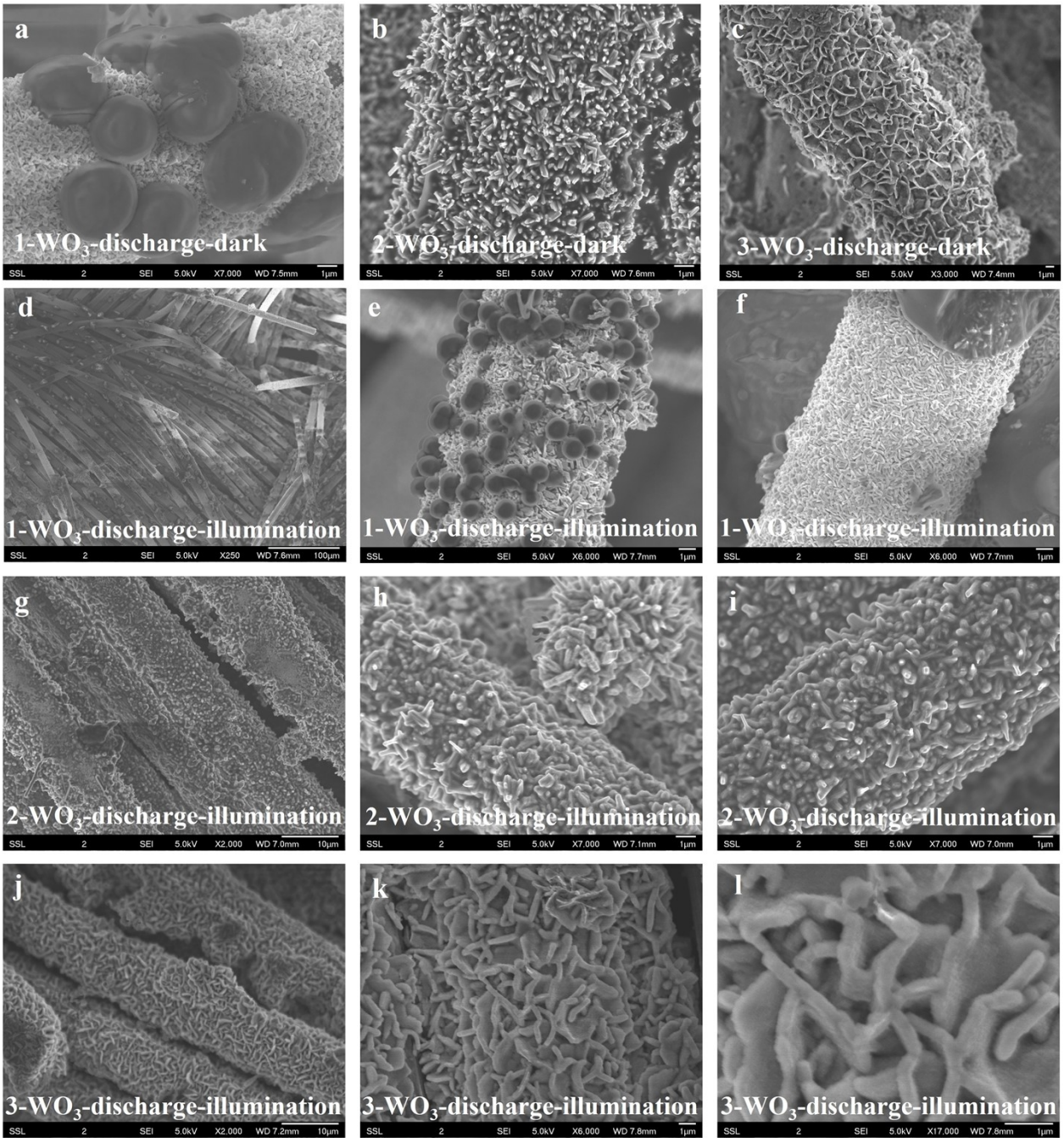

Figure S17. SEM images of (a) 1-WO_3-nanoplate/CC, (b) 2-WO_3-nanorod/CC and (c) 3-WO_3-nanosheet/CC after full discharge process under dark condition at a current density of 50 mA g^{-1} (0.02 mA/cm^2). SEM images of (d-f) 1-WO_3-nanoplate/CC, (g-i) 2-WO_3-nanorod/CC and (j-l) 3-WO_3-nanosheet/CC after full discharge process under illumination at a current density of 50 mA g^{-1} (0.02 mA/cm^2).

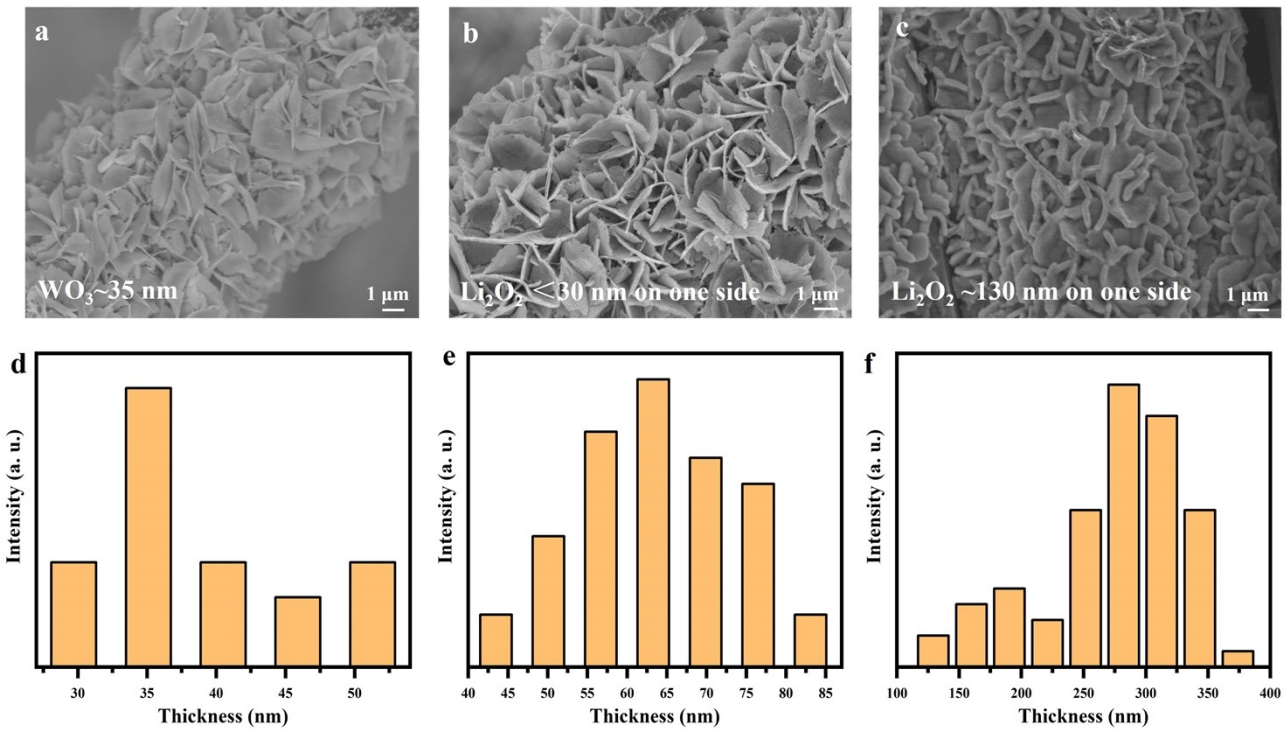

Figure S18. SEM image of (a) pure 3-WO_3 nanosheet, (b) 3-WO_3 nanosheet after full discharge process in the dark and (c) 3-WO_3 nanosheet after full discharge process under illumination, respectively. (d-f) the corresponding thickness distribution statistics.

The distribution statistics were obtained by counting about 100 edge thicknesses in the SEM images. **Fig. S18 d-e** exhibit that the average edge thicknesses of pure 3-WO_3, and 3-WO_3 after the full discharge process without and with illumination are distributed at 35, 65-70, and 300 nm, respectively. After deducting the value of pure 3-WO_3, the thicknesses of Li_2O_2 on one side of the WO_3 nanosheet without and with illumination are 17.5 and 132.5, respectively. Besides, the TEM images in **Fig. 6 b-c** (insert picture) also provide consistent results, in which Li_2O_2 can grow to 12-27 nm (dark conditions) and 130 nm (under illumination), respectively. Therefore, the thicknesses of film-like Li_2O_2 after the full discharge process are finally determined to be ＜30 nm in the dark and ~130 nm under illumination.

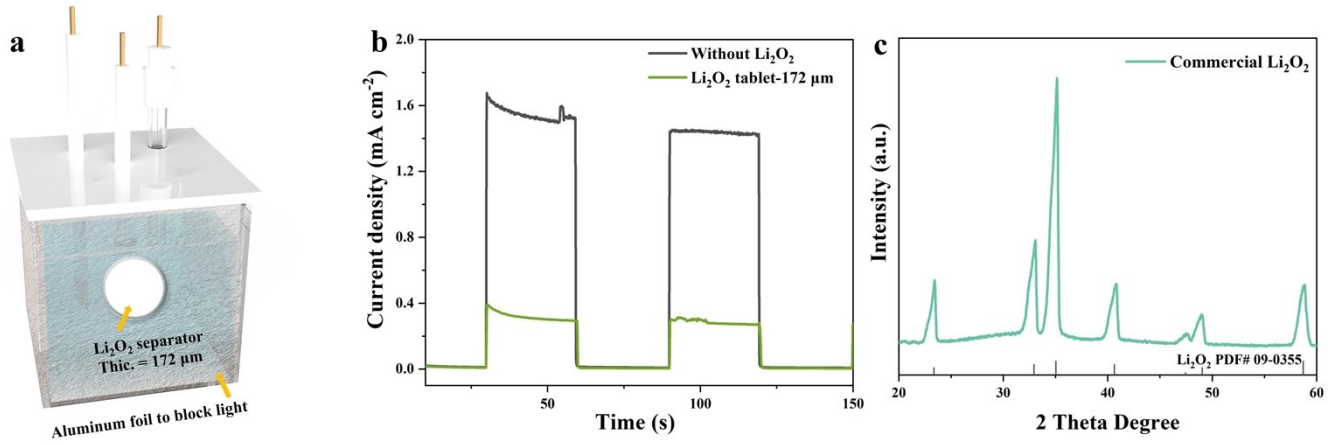

Figure S19. (a) Experimental setup for the light penetration ability of Li_2O_2. (b) I-t curves of pure 3-WO_3 and after placed commercial Li_2O_2 separator between WO_3 and Xe lamp (0.5M $NaSO_4$ solution, 1 V vs Ag/AgCl). (c) XRD curve of the tested commercial Li_2O_2.

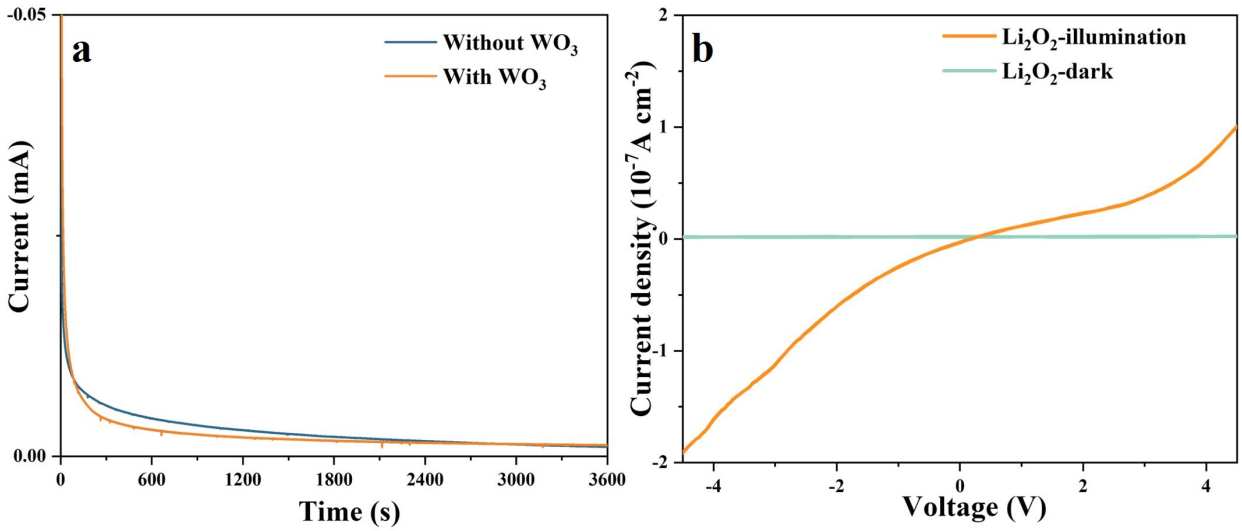

Figure S20. (a) Current contributed by the surface route during the potentiostatic discharge at 2.5 V vs Li^+/Li. (b) The current-voltage (I-V) curves of commercial Li_2O_2 with and without illumination (I-V measurements of the Li_2O_2 sheet have been made at room temperature in the voltage range from -4.5 V to 4.5 V in the two-electrode system)

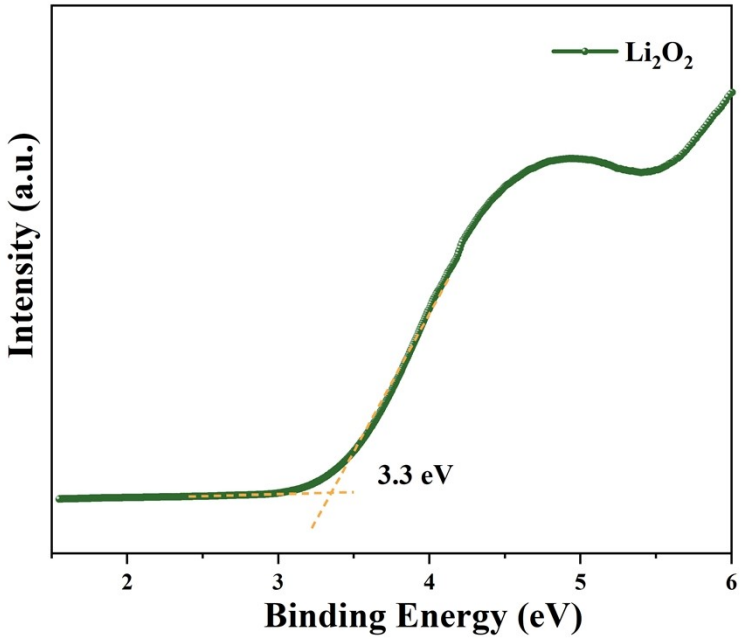

Figure S21. The Tacu plot of commercial Li_2O_2.

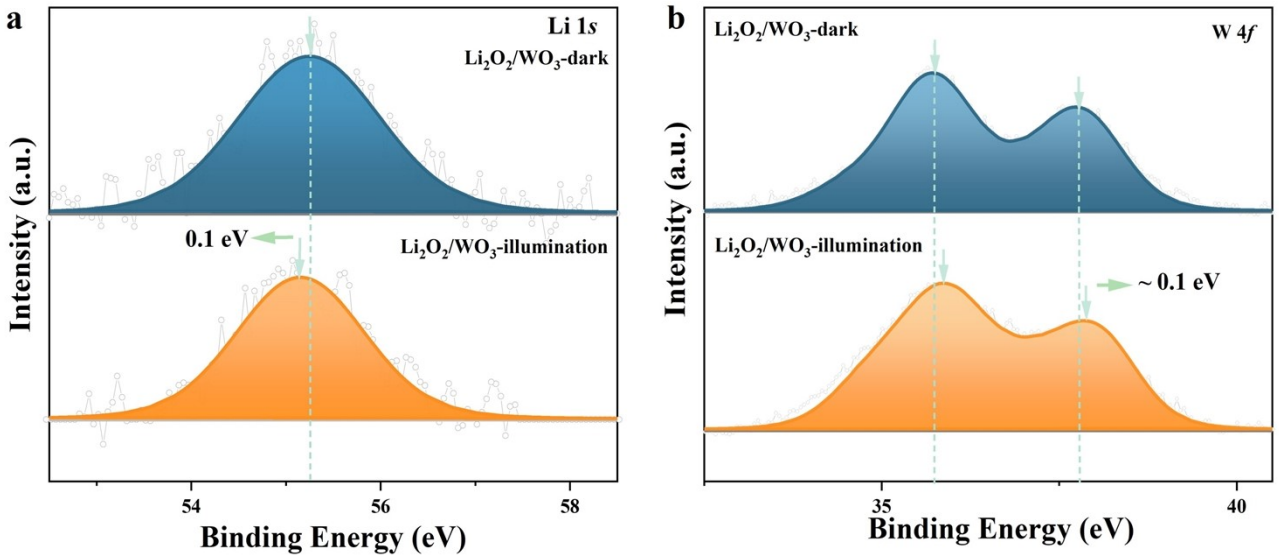

Figure S22. In situ XPS spectra for Li 1*s* and W 4*f* of Li_2O_2/WO_3 with and witnout illumination (The 3-WO_3/CC was discharged for 60 h at the current density of 50 mA/g).

References

1 J. W. Sun, A. Ruzsinszky and J. P. Perdew, *Phys. Rev. Lett.,* 2015, **115**, 036402.

2 J. W. Sun, R. C. Remsing, Y. B. Zhang, Z. R. Sun, A. Ruzsinszky, H. W. Peng, Z. H. Yang, A. Paul, U. Waghmare, X. F. Wu, M. L. Klein and J. P. Perdew, *Nat. Chem.,* 2016, **8**, 831-836.

3 J. W. Furness, A. D. Kaplan, J. L. Ning, J. P. Perdew and J. W. Sun, *J. Phys. Chem. Lett.,* 2020, **11**, 8208-8215.

4 F. Tran, J. Stelzl and P. Blaha, *J. Chem. Phys.,* 2016, **144**, 204120.

5 Y. Hinuma, H. Hayashi, Y. Kumagai, I. Tanaka and F. Oba, *Phys. Rev.B,* 2017, **96**, 094102.

6 Y. B. Zhang, D. A. Kitchaev, J. L. Yang, T. N. Chen, S. T. Dacek, R. A. Sarmiento-Pérez, M. A. L. Marques, H. W. Peng, G. Ceder, J. P. Perdew and J. W. Sun, *NPJ Comput. Mater.,* 2018, **4**, 9.

7 S. B. Zhang and J. E. Northrup, *Phys. Rev. Lett.,* 1991, **67**, 2339-2342.

8 C. G. Van de Walle and J. Neugebauer, *J. Appl. Phys.,* 2004, **95**, 3851-3879.

9 K. Mathew, R. Sundararaman, K. Letchworth-Weaver, T. A. Arias and R. G. Hennig, *J. Chem. Phys.,* 2014, **140**, 084106-084106.

10 K. Mathew, V. S. C. Kolluru, S. Mula, S. N. Steinmann and R. G. Hennig, *J. Chem. Phys.,* 2019, **151**, 234101.

11 Z. Y. Lyu, L. J. Yang, Y. P. Luan, X. R. Wang, L. J. Wang, Z. H. Hu, J. P. Lu, S. N. Xiao, F. Zhang, X. Z. Wang, F. W. Huo, W. Huang, Z. Hu and W. Chen, *Nano Energy,* 2017, **36**, 68-75.

12 W. R. Dai, Y. Liu, M. Wang, M. Lin, X. Lian, Y. N. Luo, J. L. Yang and W. Chen, *ACS Appl. Mater. Interfaces,* 2021, **13**, 19915-19926.

13 Y.-C. Wu, J. L. Ye, G. P. Jiang, K. Ni, N. Shu, P.-L. Taberna,Y. W. Zhu and P. Simon, *Angew. Chem. Int. Ed.,* 2021, **60**, 13317-13322.